Eur. Phys. J. B **50**, 393–402 (2006)
DOI: 10.1140/epjb/e2006-00153-6

THE EUROPEAN PHYSICAL JOURNAL B

Dynamics of topological solitons in two-dimensional ferromagnets

D.D. Sheka[1,a], C. Schuster[2], B.A. Ivanov[3], and F.G. Mertens[2]

[1] National Taras Shevchenko University of Kiev, 03127 Kiev, Ukraine
[2] Physics Institute, University of Bayreuth, 95440 Bayreuth, Germany
[3] Institute of Magnetism, 04071 Kiev, Ukraine

Received 14 August 2005 / Received in final form 6 January 2006
Published online 5 May 2006 –

Abstract. Dynamical topological solitons are studied in classical two-dimensional Heisenberg easy-axis ferromagnets. The properties of such solitons are treated both analytically in the continuum limit and numerically by spin dynamics simulations of the discrete system. Excitation of internal mode causes orbital motion. This is confirmed by simulations.

PACS. 75.10.Hk Classical spin models – 75.30.Ds Spin waves – 05.45.-a Nonlinear dynamics and chaos – 75.40.Mg Numerical simulation studies

1 Introduction

The analysis of two-dimensional (2D) magnetic solitons continues for more than 25 years, for reviews see references [1–3]. Such solitons are well-known to play an important role in the physics of 2D magnetic systems. In easy-plane magnets with continuously degenerated ground state there appear magnetic vortices, which are responsible for the Berezinskiĭ-Kosterlitz-Thouless phase transition [4,5]. Belavin and Polyakov were the first who constructed exact analytical solutions for 2D topological solitons in the *isotropic* magnet in the continuum limit, and proved that such solitons are responsible for the destruction of the long-range ordering for finite temperature [6]. In the *anisotropic* magnets such static solitons are unstable against collapse [7,8]. However in easy-axis magnets there appear various types of dynamical localized topological solitons due to the presence of additional integrals of motion. We will consider *precessional* solitons [1], which exist in uniaxial magnets due to the conservation of the z-projection S_z of the total spin [1,9]. Precessional solitons are known for a number of models used in field theory and condensed matter physics, see reference [10]. The topological small radius solitons become interesting now due to possible applications in high-energy physics [11] and the quantum Hall effect [12].

The problem of the dynamics of topological solitons and vortices is a complicated task for 2D ferromagnets, where Lorentz and Galilean invariance are absent. The presence of a gyroforce acting on a moving soliton is the only thing which is well established, but the free gyroscopic dynamics has not been reported till now for any 2D solitons. For the easy-plane magnets the weak localization of the vortex is related to the gapless magnon spectrum; hence the vortex dynamics is governed mostly by the interaction with the system border, and the inertial properties do not appear. As a result, computer simulations of magnetic vortex dynamics in a large but finite lattice show a motion which can be described by complicated non-Newtonian dynamical equations with nonlocal terms [13]. For the isotropic magnet with the gapless magnon dispersion law numerical analysis shows the absence of the localized motion of the soliton [14].

A very attractive candidate to discuss the general problems of the magnetic soliton motion is the easy-axis ferromagnet. In this case the soliton shape is exponentially localized, it seems to be possible to separate the soliton motion from the magnons due to their finite activation energy. The general features of the 2D soliton dynamics, which should have particle-like properties with a finite soliton mass, are not clear at present. For example, in works of Papanicolaou et al. [14–16] the dynamics of 2D solitons was described using the algebra for some noncanonic momentum. In particular, as it was mentioned in reference [15], a single topological soliton can not move without external field. At the same time a free rotational motion of the 2D topological soliton was predicted in reference [17]. It results in a finite mass for the small-radius soliton [17], while the mass of the localized soliton diverges as the logarithm of the system size according to [18].

The present work is devoted to the analysis of the dynamical properties of topological solitons in easy-axis ferromagnets, both in the discrete model with weak anisotropy and in the continuum model. We should stress

[a] e-mail: Denis_Sheka@univ.kiev.ua

here that topological solitons were studied only in the frameworks of continuum field approaches in all above mentioned papers. Spin dynamics simulations for the motionless 2D topological solitons were performed in [19]. In this paper we perform spin dynamics simulations for a wide range of soliton shapes: from large radius solitons to small ones. The main issue is to move the soliton. Using the structure of internal modes [20], we have found such perturbations of initial centrosymmetric soliton shape, which results in perfect orbital motion of the soliton.

2 Discrete model and continuum limit for 2D ferromagnets

We consider the simplest model of the classical 2D ferromagnet described by the following Hamiltonian

$$\mathcal{H} = -\frac{J}{2}\sum_{(\boldsymbol{n},\boldsymbol{\alpha})}\left(\boldsymbol{S}_{\boldsymbol{n}}\cdot\boldsymbol{S}_{\boldsymbol{n}+\boldsymbol{\alpha}} + \delta S^z_{\boldsymbol{n}} S^z_{\boldsymbol{n}+\boldsymbol{\alpha}}\right). \tag{1}$$

Here $\boldsymbol{S}_{\boldsymbol{n}} \equiv (S^x_{\boldsymbol{n}}, S^y_{\boldsymbol{n}}, S^z_{\boldsymbol{n}})$ is a classical spin vector with fixed length S (in units of the Plank constant $\hbar$) on the site $\boldsymbol{n}$ of a two-dimensional square lattice, $\boldsymbol{\alpha}$ is a vector to a nearest neighbor. The model includes the isotropic Heisenberg exchange interaction, $J > 0$ is the exchange integral, and the spatially homogeneous uniaxial exchange anisotropy, δ is the anisotropy constant. The summation runs over nearest-neighbor pairs $(\boldsymbol{n}, \boldsymbol{n}+\boldsymbol{\alpha})$. The case $\delta = 0$ corresponds to the isotropic model. To describe the anisotropy effects we will consider the case when $\delta > 0$, then the z-axis suppose the easiest magnetization.

The spin dynamics is described by the discrete version of the Landau-Lifshitz equations

$$\frac{d\boldsymbol{S}_{\boldsymbol{n}}}{dt} = -\frac{1}{\hbar}\left[\boldsymbol{S}_{\boldsymbol{n}} \times \frac{\partial \mathcal{H}}{\partial \boldsymbol{S}_{\boldsymbol{n}}}\right]. \tag{2}$$

The model of the pure uniaxial ferromagnet has well-known linear excitations (magnons) above the ground state $\boldsymbol{S}^z_{\boldsymbol{n}} = 1$ of the form $1 - \boldsymbol{S}^z_{\boldsymbol{n}} = \text{const} \ll 1$, $\boldsymbol{S}^x_{\boldsymbol{n}} + i\boldsymbol{S}^y_{\boldsymbol{n}} \propto \exp(ik_x a + ik_y a - i\omega t)$, which have the finite gap dispersion law

$$\omega(\boldsymbol{k}) = \omega_0 + \frac{4JS}{\hbar}\left[\sin^2\left(\frac{k_x a}{2}\right) + \sin^2\left(\frac{k_y a}{2}\right)\right]. \tag{3}$$

Here $\omega_0 = 4JS\delta/\hbar$ is the homogeneous ferromagnetic resonance frequency, $\boldsymbol{k}$ is the wave vector.

In the case of weak anisotropy, $\delta \ll 1$, the characteristic size $l_0 = a/\sqrt{4\delta}$ of the excitations is larger than the lattice constant a, so that in the lowest approximation in the small parameter a/l_0 and with weak gradients of magnetization one can use the continuum approximation for the Hamiltonian (1) by introducing the normalized spin $\boldsymbol{s} = \boldsymbol{S}/S = (\sin\theta\cos\phi; \sin\theta\sin\phi; \cos\theta)$. The continuum version of the Hamiltonian is

$$\mathcal{E}[\theta,\phi] = \frac{JS^2}{2}\int d^2x\left[(\nabla\theta)^2 + \sin^2\theta\,(\nabla\phi)^2 + \frac{\sin^2\theta}{l_0^2}\right]. \tag{4}$$

In terms of the fields θ and ϕ, the Landau-Lifshitz equations (2) read

$$\sin\theta\;\partial_t\phi = -\frac{a^2}{\hbar S}\frac{\delta\mathcal{E}}{\delta\theta}, \qquad \sin\theta\;\partial_t\theta = \frac{a^2}{\hbar S}\frac{\delta\mathcal{E}}{\delta\phi}. \tag{5}$$

In the long wavelength limit the magnon excitations of the form $\theta = \text{const} \ll 1$, $\phi = \boldsymbol{k}\cdot\boldsymbol{r} - \omega t$, have the following dispersion law,

$$\omega(\boldsymbol{k}) = \omega_0(1 + k^2 l_0^2), \tag{6}$$

which follows from (3) in the lowest approximation in $ka \ll 1$.

3 The structure of precessional soliton

For the pure uniaxial ferromagnet the Hamiltonian (1) does not depend explicitly on the variable ϕ due to the spin-space isotropy (in contrast to the lattice, which is always anisotropic but in coordinate space). This condition corresponds to the additional integral of motion

$$N = \sum_{\boldsymbol{n}}\left(S - S^z_{\boldsymbol{n}}\right). \tag{7}$$

When $N \gg 1$ and the WKB approach is valid, one can consider $N \in \mathbb{N}$ as the number of magnons, bound in the soliton, see reference [1]. The conservation law (7) can provide a conditional minimum of the Hamiltonian, which stabilize the possible soliton solution, see below. The continuous version of (7) reads

$$N = \frac{S}{a^2}\int d^2x\,(1 - \cos\theta). \tag{8}$$

The simplest nonlinear excitation of the model (5) is a 2D soliton, which has a finite energy. The topological properties of the soliton are determined by the mapping of the xy-plane to the S^2-sphere of the order parameter space. This mapping is described by the homotopic group $\pi_2(S^2) = \mathbb{Z}$, which is characterized by the topological invariant (Pontryagin index)

$$q = \frac{1}{4\pi}\int d^2x\mathcal{Q}, \qquad \mathcal{Q} = \frac{\varepsilon_{\alpha\beta}}{2}\Big[\boldsymbol{s}\cdot\left(\nabla_\alpha\boldsymbol{s}\times\nabla_\beta\boldsymbol{s}\right)\Big]. \tag{9}$$

The Pontryagin index takes integer values, $q \in \mathbb{Z}$, being an integral of motion.

Let us consider the so-called *centrosymmetric topological precessional soliton*, which has the following structure:

$$\theta = \theta_0(\rho), \qquad \phi = \varphi_0 + q\chi - \omega_p t, \tag{10}$$

where $\rho = r/l_0$ is the dimensionless radius and $\omega_p \in (0, \omega_0)$ is the frequency of the internal precession. We will discuss only the case $q = 1$, when the soliton has a lower energy. The form of the function $\theta_0(\bullet)$ satisfies the following differential problem:

$$\frac{d^2\theta_0}{d\rho^2} + \frac{1}{\rho}\frac{d\theta_0}{d\rho} - \sin\theta_0\cos\theta\left(1 + \frac{1}{\rho^2}\right) + \frac{\omega_p}{\omega_0}\sin\theta_0 = 0, \tag{11a}$$

$$\theta_0(0) = \pi, \qquad \theta_0(\infty) = 0. \tag{11b}$$

This equation was solved numerically in references [21–23]. For the case of a centrosymmetric soliton the number of bound magnons

$$N = N_0 \int_0^\infty \rho\, d\rho \left[1 - \cos\theta_0(\rho)\right], \tag{12}$$

where $N_0 = 2\pi S l_0^2/a^2$ is the characteristic number of bound magnons for 2D magnets [21]. Multiplying equation (11a) by $\rho^2 d\theta_0/d\rho$ and integrating over all ρ, one can easily obtain the identity

$$\int_0^\infty \sin^2\theta_0(\rho)\rho d\rho = \frac{2\omega_p}{\omega_0}\int_0^\infty \left[1-\cos\theta_0(\rho)\right]\rho d\rho, \tag{13}$$

which gives a possibility to rewrite the soliton energy (4) as follows

$$\mathcal{E} = \mathcal{E}_{\rm exc} + \hbar\omega_p N,$$
$$\mathcal{E}_{\rm exc} = \frac{JS^2}{2}\int d^2x \left[(\nabla\theta)^2 + \sin^2\theta\,(\nabla\phi)^2\right]. \tag{14}$$

Note that the linear dependence of the soliton energy $\mathcal{E}$ on N agrees with the general relation $\hbar\omega_p = \delta\mathcal{E}/\delta N$.

The shape of the soliton essentially depends on the number N of bound magnons. In the case of solitons with large radius R (equivalent to $N \gg N_0$), the approximate "domain wall" solution works well, see reference [1]. This solution has the shape of a curved 1D domain wall at the distance R

$$\cos\theta_0(r) = \tanh\frac{r-R}{l_0}. \tag{15}$$

Using this simple structure one can obtain the number of bound magnons, which is proportional to the area of the soliton, $N \approx N_0(R/l_0)^2$, and precession frequency

$$\frac{\omega_p}{\omega_0} \approx \frac{l_0}{R} \approx \sqrt{\frac{N_0}{N}}. \tag{16}$$

In the case of small radius solitons ($N \ll N_0$), the following asymptotically exact solution works well [23]

$$\tan\frac{\theta_0(r)}{2} = \frac{R}{r_0}\,K_1\left(\frac{r}{r_0}\right), \qquad r_0 = \frac{l_0}{\sqrt{1-\omega_p/\omega_0}}, \tag{17}$$

where $K_1(\bullet)$ is the McDonald function. It provides correct behavior for $r < R \ll l_0$, where it converts to the Belavin-Polyakov solution $\tan\theta_0/2 = R/r$ and provides a correct exponential decay for $r \gg R$. In this case the frequency of the soliton precession $\omega_p \to \omega_0$ when $N \to 0$, but the dependence $\omega_p(N)$ has a singularity at the origin: $d\omega_p/dN \to \infty$ as $N \to 0$

$$\frac{\omega_p}{\omega_0} \approx 1 - \frac{1}{\ln\left(8N_0/e\gamma^2 N\right)}, \tag{18}$$

where $\gamma \approx 1.78$ is the Euler constant, see references [23,24].

In the intermediate case of arbitrary R, it is possible to use an approximate trial function of the form, proposed in reference [20],

$$\tan\frac{\theta_0(r)}{2} = \frac{R}{r}\exp\left(-\frac{r-R}{r_0}\right). \tag{19}$$

Here R is the fitting parameter, which was found in reference [20] by fitting the trial function (19) to the numerical solution of the differential problem (11). The value of this fitting parameter is closed to the soliton radius, which satisfies the condition $\cos\theta_0(R) = 0$.

The trial function (19) gives a possibility to describe approximately the soliton shape for a given radius R. However, it contains one extra parameter, ω_p, due to the dependence $r_0 = r_0(\omega_p)$. One can calculate approximately the $\omega_p(R)$-dependence as follows

$$\omega_p(R) \approx \frac{\omega_0 l_0}{R + l_0}, \tag{20}$$

which provides the correct asymptote (16) for $R \gg l_0$ and gives the limiting value $\omega_p = 0$ for $R \ll l_0$. In the same approach the typical size of the exponential tail of the soliton $r_0 \approx l_0\sqrt{(R+l_0)/R}$; thus for the soliton shape we have finally

$$\tan\frac{\theta_0(r)}{2} \approx \frac{R}{r}\exp\left(-\frac{r-R}{l_0}\sqrt{\frac{R}{R+l_0}}\right),$$
$$\phi = \varphi_0 + \chi - \omega_p t. \tag{21}$$

We will use this simple expression as initial condition for our numerical simulations in Section 5.

4 The soliton dynamics

To describe the dynamics of the soliton as a whole, it is necessary first of all to introduce an effective soliton coordinate. Let us define the soliton position $\boldsymbol{X}(t) = X(t) + iY(t)$ as the center of mass of the z-component of the magnetization field:

$$\boldsymbol{X}(t) = \frac{S}{Na^2}\int d^2x\; \boldsymbol{r}\,(1-\cos\theta). \tag{22}$$

Using this quantity we will look for the way of possible soliton deformation, which initialize its motion. In order to realize this idea, let us derive the soliton speed (see Appendix A):

$$\frac{d\boldsymbol{X}}{dt} = \frac{JS^2}{\hbar N}\int d^2x \sin^2\theta \boldsymbol{\nabla}\phi. \tag{23}$$

It is convenient to classify all possible perturbations of the soliton shape using a complete set of functions. We choose the solution of the linearized problem, which provides a set of partial waves.

Let us remind that the soliton in an easy-axial ferromagnet has a number of local magnon modes. The existence of local modes is possible because of the gap in

the magnon spectrum as predicted in reference [20]; such modes correspond to different types of soliton shape oscillations. To describe the local modes one has to linearize the Landau-Lifshitz equations (5) on the soliton background as it was done in reference [20]. We use the partial-wave expansion

$$\theta = \theta_0(\rho) + \sum_m A_m \left(u_m + v_m\right) \cos \Phi_m,$$

$$\phi = \varphi_0 + \chi - \omega_p t + \sum_m \frac{A_m}{\sin\theta_0} \left(u_m - v_m\right) \sin \Phi_m, \quad (24)$$

where $\Phi_m = m\chi - \omega_m t$ and ω_m is the magnon frequency in the rotating frame. The radial functions $u_m(\rho)$ and $v_m(\rho)$ satisfy the following eigenvalue problem for two coupled Schrödinger-like equations:

$$\left[-\frac{d^2}{d\rho^2} - \frac{1}{\rho}\frac{d}{d\rho} + V_+(\rho) - \frac{\omega_m}{\omega_0}\right] u_m = W(\rho) v_m,$$

$$\left[-\frac{d^2}{d\rho^2} - \frac{1}{\rho}\frac{d}{d\rho} + V_-(\rho) + \frac{\omega_m}{\omega_0}\right] v_m = W(\rho) u_m, \quad (25)$$

where the radial "potentials" are

$$V_\pm(\rho) = \frac{(\cos\theta_0 \pm m)^2}{\rho^2} + \cos\theta_0 \left(\cos\theta_0 - \frac{\omega_p}{\omega_0}\right) - \frac{1}{2}\sin^2\theta_0 \left(1 + \frac{1}{\rho^2}\right) - \frac{1}{2}(\theta_0')^2,$$

$$W(\rho) = \frac{1}{2}\sin^2\theta_0 \left(1 + \frac{1}{\rho^2}\right) - \frac{1}{2}(\theta_0')^2.$$

The local modes exist in a range of frequencies inside the gap, $\omega_m^{\rm loc} \in (0, \omega_0 - \omega_p)$. The number of local modes essentially depends on the soliton radius: when the soliton radius decreases, the local modes leave the gap range, transforming to the quasi-local modes with singularities in the scattering picture. For the soliton with $R \leq R_c = 1.52 l_0$ there exists only one local mode, namely the mode with $m = -1$, and it is this mode which corresponds to the soliton motion.

Let us calculate the effective soliton trajectory $\boldsymbol{X}(t)$ using the partial wave ansatz (24). In the linear approximation in A_m all modes with $|m| \neq 1$ give no contribution to the integral (23) due to the angular symmetry, and the effective soliton coordinate results as follows (see Appendix A for the details)

$$\boldsymbol{X}(t) = R_{\rm orb} e^{-i\omega_{-1}t},\ R_{\rm orb} = \frac{|A_{-1}|\ |C_{-1}|\, N_0 \omega_0 l_0}{2N\omega_{-1}},$$

$$C_{-1} = 4\int_0^\infty \rho d\rho \cos\theta_0 \Big(u_{-1}v_1 - v_{-1}u_1\Big). \quad (26)$$

Thus, only the perturbation with the symmetry of the mode $m = -1$ can lead to a soliton motion as a whole. As we have found, the best way to excite such a mode is to use the exact shape of this mode, calculated in linear approximation, with *finite* amplitude of deformation A_{-1}. We will check this prediction in Section 6.

At the end of the section let us discuss the connection between the dynamics of the soliton center $\boldsymbol{X}(t)$, which results in the orbital motion (26), and the dynamics of the specific soliton position, introduced by Papanicolaou and Tomaras [15] as a some integral of the topological density $\mathcal{Q}$ (9):

$$\boldsymbol{R} = \frac{\int d^2x \boldsymbol{r}\mathcal{Q}}{\int d^2x \mathcal{Q}}. \quad (27)$$

This quantity can be interpreted as a "guiding center" of the soliton orbit. In the linear on A_m approximation one can calculate (see Appendix A) that

$$\boldsymbol{R}(t) = -A_1 l_0 \boldsymbol{e}_x = \text{const.}, \quad (28)$$

which corresponds to the simple soliton shift due to the translational mode with $m = +1$. The physical picture is similar to the electron motion in the magnetic field: the electron moves along the circular Larmor orbit and $d\boldsymbol{X}/dt$ is not conserved; the generalized momentum $\boldsymbol{P}$ also changes; however their combination, which determine the center of the "guiding center" of the orbit $\boldsymbol{R}$ saves its position.

5 Numerical simulations for the circular symmetric topological precessional soliton

To validate predictions of the continuum theory for the soliton properties, we integrate numerically the discrete Landau-Lifshitz equations (2) over square lattices of size $L \times L$ using a 4th-order Runge-Kutta scheme with time step 0.01 and periodic boundary conditions. In all cases the soliton is started near the center of the domain. We have fixed the exchange constant $J = \hbar = 1$ as well as the spin length $S = 1$. We have considered the anisotropy parameter in the range $\delta \in (0.0005; 0.1)$, corresponding to $l_0/a \in (22.4, 1.58)$ so that we are close to the continuum limit. We consider system sizes in the range $L/a \in (50, 800)$.

We start the simulations using an initial soliton-like distribution

$$\theta = \theta_0(r), \quad \phi = \varphi_0 + \chi, \quad (29)$$

with the trial function (21) for the θ-field. Evidently, the soliton solutions of the Landau-Lifshitz equations for a lattice differ from the circular symmetric continuous solutions, and also from the simple trial function. To find such a "pure" soliton solution, i.e. to adapt the trial solution to the lattice, one should provide enough time for the decay of the initial error in the trial functions. In fact, using (29) as initial conditions for the lattice we excite also magnons, which should be taken out the system. To avoid the problem of magnons we have damped them the initial stage of simulations by applying damping. This kills all spreading spin waves coming from the imperfect initial condition. In

this way instead of equations (2), we have integrated numerically Landau-Lifshitz equations with Gilbert damping

$$\hbar(1+\varepsilon^2)\frac{d\boldsymbol{S_n}}{dt} = -\left[\boldsymbol{S_n}\times\frac{\partial\mathcal{H}}{\partial\boldsymbol{S_n}}\right]+\frac{\varepsilon}{S}\left[\boldsymbol{S_n}\times\left[\boldsymbol{S_n}\times\frac{\partial\mathcal{H}}{\partial\boldsymbol{S_n}}\right]\right],$$

see reference [25] for details. The lowest frequency of the continuous magnon spectrum is ω_0, thus the damping time $t_d \approx 1/(\varepsilon\omega_0)$, see reference [19] for details. During the damping time ($t < t_d$), the magnons are damped in the system, but the soliton is also damped, and the soliton energy $\mathcal{E}$ decays as well as the number of bound magnons N. In order to save the soliton structure, we should switch off the damping before we damp out the soliton, i.e. $t < 1/\varepsilon\omega_p$. In all simulations we use the same value of $\varepsilon = 0.02$, then the damping time $t_d \approx 12/\delta$, and the damping is turned off *adiabatically* after a time greater than t_d.

Let us discuss the choice of the other parameters. In all simulations we want to be not far from the continuum limit in order to validate the continuum approach. It means that the magnetic length l_0 should be greater than the lattice constant a. This regulates the choice of the anisotropy constant $\delta = a^2/4l_0^2$. Besides l_0 the soliton shape is characterized by two extra scales: R, which is the soliton radius, and r_0, which characterizes the scale of the exponential decay of the excitation far from the soliton center.

We start with the large radius solitons. In this case $R \gg r_0 \approx l_0$, and we can limit ourselves by choosing $\delta = 0.1$ (this corresponds to $l_0 \approx 1.6a$). The system size L should be much greater than the largest parameter of the soliton, which is its radius. We consider solitons up to the radius $R = 20l_0 \approx 31.6a$. Thus we consider lattices with $L = 200a$, which satisfy all above mentioned conditions.

In the case of small radius solitons we have the following relation between the parameters of the system:

$$a \ll R \ll l_0 \ll r_0 \ll L. \tag{30}$$

For the smallest soliton we choose $\delta = 0.0005$, which corresponds to $l_0 \approx 22.4a$; this gives the possibility to consider solitons of small radii down to $R = 0.225l_0 \approx 5a$. However, such a small anisotropy drastically changes the soliton shape far from the center, which has the scale r_0, see equation (17). For example, for the soliton with $R = 0.225l_0$, the precession frequency $\omega_p \approx 0.84\omega_0$ (see Ref. [20]), which results in $r_0 = l_0/\sqrt{1-\omega_p/\omega_0} \approx 56a$. Thus to consider small radius solitons we must increase the system size. In our spin dynamics simulations we choose $L = 800a$ for the smallest solitons. To perform simulations for such large systems, 800×800, we have used parallelize a computations, see Appendix B.

Let us discuss results of our spin dynamics simulations. Starting from initial conditions (29), and adapting the soliton shape to the lattice, we have obtained the class of one-parameter stable soliton solutions for a wide range of the parameter N, or equivalently, the soliton radius R. We have studied the $R(N)$ dependence, which is presented in Figure 1. Almost in the full range of parameters, the

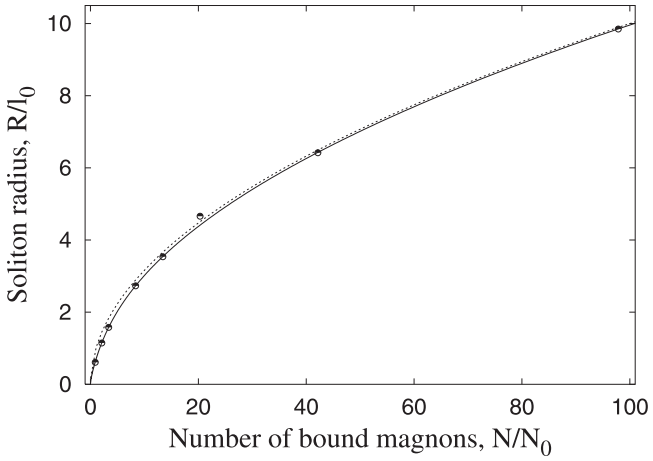

Fig. 1. Soliton radius as a function of the number of bound magnons. The symbols correspond to the simulation data; the solid line is the result of the numerical integration of the continuum limit equations (11), (12) using the one-parameter shooting method with the 4th-order Runge-Kutta scheme. The dashed line corresponds to equation (31).

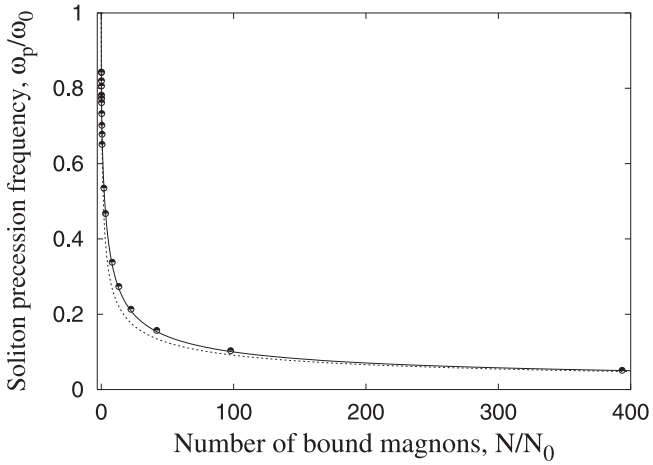

Fig. 2. Soliton precession frequency as a function of the number of bound magnons. Symbols correspond to the simulation data; the solid line is the result of continuum model integration; the dashed line corresponds to equation (32).

simple dependence

$$N \approx N_0\left(\frac{R}{l_0}\right)^2 \tag{31}$$

is valid. Note that the dependence (31) was verified numerically in reference [19] for the large radius solitons only, where $R > 10l_0$. Here we want to check the continuum results for arbitrary R. Using (20) and (31), an approximate dependence

$$\omega_p(N) \approx \frac{\omega_0}{1+\sqrt{N/N_0}} \tag{32}$$

can be derived. To compute the precession frequency, we calculate the Fourier spectrum of the in-plane spin components. One can see from Figure 2 that this simple dependence works well in a wide range of parameters.

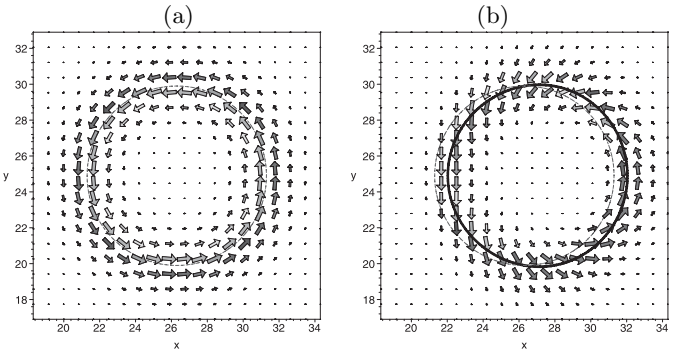

Fig. 3. In-plane spin distribution for the soliton with $R = 5l_0$, which is situated at $\boldsymbol{X}_0 = 26.3 + i25.0$. (a) corresponds to the circular symmetric soliton and (b) to an elliptically deformed one. The lines describe the contour plot of $S_z = 0$ ($\theta = \pi/2$): the dashed line is for the circular symmetric soliton and the solid line is for the deformed soliton.

6 Simulation of the orbital motion of the soliton

In the previous section we have performed spin dynamics simulations only for the circular symmetric precessional soliton, which does not move as a whole. As mentioned in Section 4, in order to move the soliton one should break its symmetry. We have done this by an initial deformation of the soliton shape, and integrated numerically the Landau-Lifshitz equations. Specifically, we have chosen an elliptic kind of deformation, which corresponds to the shape of the internal partial mode with azimuthal quantum number $m = -1$. We start the simulations with initial conditions

$$\theta = \theta_0(\rho) + A[u_{-1}(\rho) + v_{-1}(\rho)]\cos\chi,$$
$$\phi = \varphi_0 + \chi - \frac{A}{\sin\theta_0}[u_{-1}(\rho) - v_{-1}(\rho)]\sin\chi \qquad (33)$$

by the same numerical scheme as described in the previous section. We calculated the functions $u_{-1}(\rho)$ and $v_{-1}(\rho)$ numerically solving the eigenvalue problem (25) by the two-parametric shooting scheme as described in reference [20]. The parameter A is the amplitude of the eigenmode, which characterizes the magnitude of the soliton deformation. An initial distribution of spins, which corresponds to equations (33), is shown in Figure 3 and can be seen to describe the elliptical kind of the soliton deformation.

During the simulations we have computed the time dependence of the position $\boldsymbol{X}(t) = \big(X(t), Y(t)\big)$ of the soliton center:

$$\boldsymbol{X}(t) = \frac{\sum_{\boldsymbol{n}} \boldsymbol{r}_{\boldsymbol{n}}\,[S - S^z_{\boldsymbol{n}}(t)]}{\sum_{\boldsymbol{n}} S - S^z_{\boldsymbol{n}}(t)}, \qquad (34)$$

which is the discrete analogue of equation (22); $\boldsymbol{r}_{\boldsymbol{n}} = (x_n, y_n)$ are the lattice points.

We have found numerically that after switching off the damping, the soliton reaches very fast a circular trajectory, see Figure 4. This results in a nice circular motion with constant frequency. For small deformations the radius of the orbit is proportional to the initial deformation. One can say that the effect of a circular motion and the excitation of the mode with $m = -1$ are identical for this case, as predicted by Sheka et al. [20]. Such a relation is valid in some range of the soliton deformation for all soliton radii, see Figure 5. Then, for larger deformations, non-linear regime is clearly seen, see Figure 6. The frequency of this orbit motion of the soliton approximately corresponds to the frequency of the local mode, $\Omega_{\rm orb} = \omega_{m=-1}$.

The presence of such an exact circular motion, with only one frequency, independent of the orbit radius (even

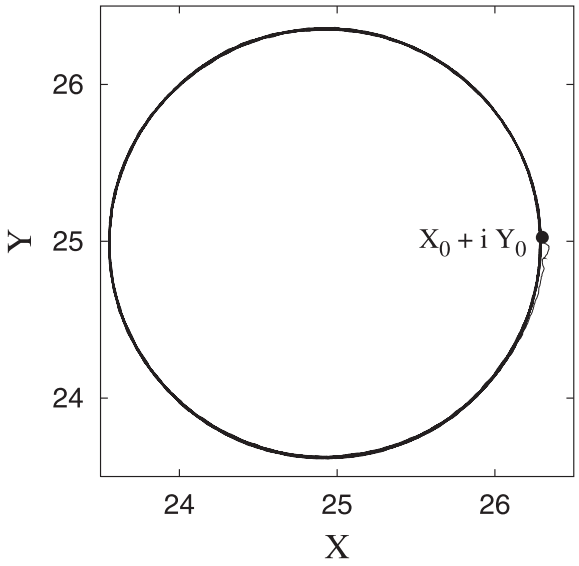

Fig. 4. Trajectory of the soliton with initial radius $R = 4.87l_0$ and initial precession frequency $\omega_p = 0.2\omega_0$. The initial point $X_0 + iY_0$ corresponds to the center of the soliton from Figure 3.

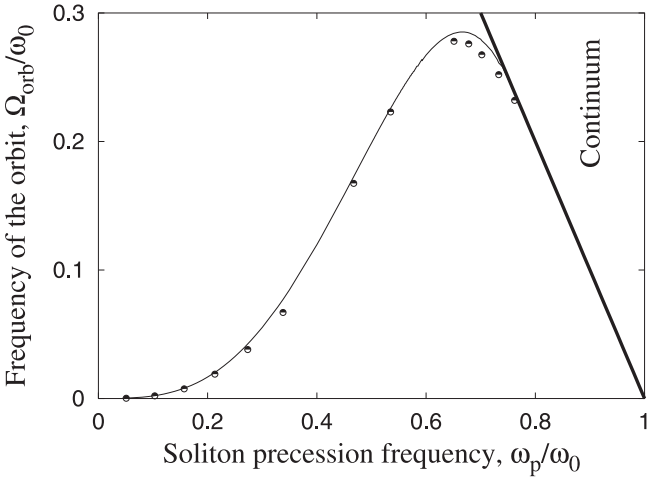

Fig. 5. Frequency of the orbit motion as a function of the precession frequency of the soliton. Symbols correspond to the spin dynamics simulation data; lines corresponds to the frequency of the eigenmode with $m = -1$ from the continuum theory by Sheka et al. [20].

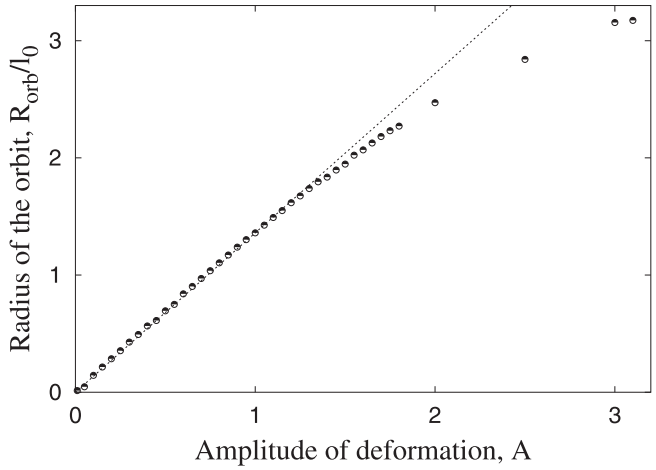

Fig. 6. Radius of the soliton orbit as a function of the deformation amplitude A. Parameters of the soliton: initial radius $R = 4.87l_0$ and initial precession frequency $\omega_p = 0.2\omega_0$.

in non-linear regime), gives the possibility to conclude that this is the *first* observation in the numerical experiment of the pure gyroscopic motion, which is equivalent to the Larmor precession of a charged particle in a magnetic field. Therefore, the soliton motion can be described by an effective equation of motion for the position of the soliton $\boldsymbol{X}$, which takes the form of usual Newtonian equation for a particle with the *well-defined effective mass* M under the influence of the gyroscopic force $\boldsymbol{F}_g$:

$$M\frac{d^2\boldsymbol{X}}{dt^2} = \boldsymbol{F}_g, \qquad \boldsymbol{F}_g = G\left[\boldsymbol{e}_z \times \frac{d\boldsymbol{X}}{dt}\right]. \tag{35}$$

Here $G = 4\pi\hbar S/a^2$ is the gyroconstant, see [1]. Formally, equation (35) has two solutions. One solution, $\boldsymbol{X} = \text{const.}$, corresponds to the translation mode with $m = +1$. In the infinite system this is a zero-frequency local mode, which describes a simple shift of the soliton, $\omega_{m=+1} = 0$. The second solution describes a circular motion with the frequency $\Omega_{\text{orb}} = G/M$. Thus, we can calculate the effective mass of the soliton using the simulation data for the orbit frequency.

We have checked how the orbit frequency depends on the soliton radius. For the large radius solitons $\Omega_{\text{orb}} \approx 2\omega_0(l_0/R)^3$ is in good agreement with the results for the local modes. For the small radius solitons, the orbit frequency tends to the boundary of the spectrum in the rotating frame, $\Omega_{\text{orb}} \approx \omega_0 - \omega_p$. This dependence corresponds to our result for the eigenfrequencies, see equation (26) of reference [20]. In the case $N \ll N_0$ one can use the approximate limiting expression (18) for ω_p, which results in

$$\Omega_{\text{orb}} \approx \omega_0 - \omega_0\left[1 - \frac{1}{\ln\left(8N_0/e\gamma^2 N\right)}\right] = \frac{\omega_0}{\ln\left(8N_0/e\gamma^2 N\right)}. \tag{36}$$

This frequency tends to zero when $R \to 0$.

One can calculate the effective mass of the soliton by $M = G/\Omega_{\text{orb}}$,

$$M = M_0 F\left(\frac{N}{N_0}\right), \qquad M_0 = \frac{G}{\omega_0} = \frac{\pi\hbar^2}{Ja^2\delta}, \tag{37}$$

where M_0 is a characteristic value of the effective mass, found in reference [17]. The function $F(\bullet) = \omega_0/\Omega_{\text{orb}}(\bullet)$ depends on the soliton size having the asymptotic behavior

$$F(x) = \begin{cases} \ln\left(\dfrac{8}{e\gamma x}\right) & \text{when } x \ll 1 \\ \dfrac{1}{2}x^{3/2} & \text{when } x \gg 1. \end{cases} \tag{38}$$

The soliton mass diverges in the limiting cases when $R \to 0$ and $R \to \infty$. Note that for the large radius solitons the mass increases faster that the domain wall width, which is proportional to R. The mass takes a minimum value $M_c \approx 3.51M_0$ for the soliton with $R_c \approx 0.547l_0$. The soliton with these parameters has the highest *mobility*.

7 Conclusion

In this paper we have studied the dynamics of topological solitons in classical 2D easy-axis ferromagnet. The analysis was made both analytically in the continuum approximation and numerically using the spin dynamics simulations for a wide range of solitons: from large radius solitons to small ones. Our simulations were performed for small anisotropies, which corresponds to the continuum description. We have checked and confirmed a number of results from the continuum theory about the soliton structure, in particular, the connection between the number of bound magnons and the precession frequency of the spins inside the soliton.

The main issue is connected with the soliton dynamics. We have proposed a way how to move a soliton exciting one of its internal modes. To our knowledge, it is the first observation of inertial motion of 2D magnetic solitons. The effective soliton dynamics is similar to the Larmor dynamics of a charged particle in a magnetic field. By analysis of the effective soliton dynamics we extract information about the effective mass of the soliton. This mass essentially depends on the anisotropy, $M \propto 1/\delta$, and on the soliton size, having the minimum for the soliton of the radius about $0.5l_0$. In the case of large radius solitons the soliton mass increases with the increase of the soliton radius. Note that it increases faster than the number of the bound magnons, $M \approx \frac{1}{2}M_0(N/N_0)^{3/2}$. Such dependence is in a good agreements with previous results [17]; the soliton mass diverges in the limit case $R \to \infty$, which corresponds to the fact that the single domain wall can not move. When the soliton radius is smaller, the effective mass increases logarithmically with its radius, and diverges in the limit case $R = 0$. Note that the problem of inertial properties of a small radius soliton have caused a lot of discussions. According to linear

analysis [17], the soliton mass tends to some limit value $M^\star = 6\sqrt{\pi}(\pi+2)M_0 \approx 55M_0$ when $R \to 0$. At the same time our previous analysis of eigenmodes [20] shows that $M \to \infty$ at the limit case $R \to 0$. Spin dynamics simulations confirms our results on internal modes: the soliton loose its mobility when becomes very small.

We have predicted the fine circular motion of the soliton by exciting its internal mode. We believe that such phenomenon can be observed experimentally, e.g. by ac pumping. Our investigations can be important also for the quantum Hall systems, where skyrmion-type solitons are well-known to lead to the breakdown of the spin-polarized quantum Hall effect [26].

D.D. Sheka thanks the University of Bayreuth, where part of this work was performed, for kind hospitality and acknowledges support from the Alexander von Humboldt Foundation. D.D. Sheka acknowledge also the support from Deutsches Zentrum für Luft- und Raumfart e.V., Internationales Büro des BMBF in the frame of a bilateral scientific cooperation between Ukraine and Germany, project No. UKR 05/055. C. Schuster thanks Stefan Karpitschka for his kind support concerning aspects of parallelizing the source code.

Appendix A: Calculation of the soliton velocity

In order to check the possible soliton motion we calculate the speed of the effective soliton position $\boldsymbol{X}(t)$. According to the equation (22) the soliton speed

$$\frac{dX_i}{dt} = \frac{S}{Na^2}\int d^2x\; x_i \sin\theta\partial_t\theta = \frac{1}{\hbar N}\int d^2x\; x_i\frac{\delta\mathcal{E}}{\delta\phi},$$

where we used the Landau-Lifshitz equation (5). Calculating the functional derivative for the energy functional (4) and integrating by parts using the identity

$$x_i\boldsymbol{\nabla}\cdot\left(\sin^2\theta\boldsymbol{\nabla}\phi\right) = \boldsymbol{\nabla}\cdot\left(x_i\sin^2\theta\boldsymbol{\nabla}\phi\right) - \sin^2\theta\partial_i\phi,$$

one can derive the soliton velocity in the form

$$\frac{d\boldsymbol{X}}{dt} = \frac{2\pi l_0 JS^2}{\hbar N}\int_0^\infty \rho d\rho\Big\langle\sin^2\theta\boldsymbol{\nabla}_{\boldsymbol{\rho}}\phi\Big\rangle, \qquad (A.1)$$

which is equivalent to equation (23). Here the averaging means $\big\langle F(\bullet,\chi)\big\rangle \equiv (1/2\pi)\int_0^{2\pi} F(\bullet,\chi)d\chi$.

Using the partial-wave ansatz (24), one can concretize the average value in equation (A.1):

$$\Big\langle\sin^2\theta\boldsymbol{\nabla}_{\boldsymbol{\rho}}\phi\Big\rangle = \sum_m A_m\Bigg\{\sin^2\theta_0\left[\frac{u_m-v_m}{\sin\theta_0}\right]'\Big\langle\sin\Phi_m e^{i\chi}\Big\rangle$$
$$+\frac{i}{\rho}\left[(u_m+v_m)\sin 2\theta_0 + m(u_m-v_m)\sin\theta_0\right]\Big\langle\cos\Phi_m e^{i\chi}\Big\rangle\Bigg\}.$$

After averaging with account of the expressions

$$\Big\langle\cos\Phi_m e^{i\chi}\Big\rangle = \frac{\delta_{|m|,1}}{2}e^{im\omega_m t}$$
$$\Big\langle\sin\Phi_m e^{i\chi}\Big\rangle = \frac{im\delta_{|m|,1}}{2}e^{im\omega_m t}, \qquad (A.2)$$

one can calculate the soliton velocity in the form

$$\frac{d\boldsymbol{X}}{dt} = \frac{i\omega_0 l_0 N_0}{2N}\Big(A_1C_1e^{i\omega_1 t} + A_{-1}C_{-1}e^{-i\omega_{-1}t}\Big), \qquad (A.3)$$

where the constants C_m are determined by the static soliton structure,

$$C_m = \int_0^\infty d\rho\Bigg\{\rho m\sin^2\theta_0\left[\frac{u_m-v_m}{\sin\theta_0}\right]' + (u_m+v_m)\sin 2\theta_0$$
$$+ m(u_m-v_m)\sin\theta_0\Bigg\}.$$

Using the equality

$$\rho\sin^2\theta_0\left[\frac{u_m-v_m}{\sin\theta_0}\right]' = [\rho(u_m-v_m)\sin\theta_0]'$$
$$-(u_m-v_m)\sin\theta_0 - 2\rho(u_m-v_m)\cos\theta_0\theta_0',$$

after the integrating the first term by parts, one can rewrite C_m as follows

$$C_m = 2\int_0^\infty \rho d\rho\left\{\frac{\sin\theta_0}{\rho}(u_m+v_m) - m\theta_0'(u_m-v_m)\right\}$$
$$= -2\int_0^\infty \rho d\rho\cos\theta_0\Bigg\{(1+m)\Big(u_mu_1 - v_mv_1\Big)$$
$$-(1-m)\Big(u_mv_1 - v_mu_1\Big)\Bigg\}. \qquad (A.4)$$

Here the mode with $m = 1$ is the zero-frequency local mode, which describes a shift of the soliton position, its eigenspectrum has the form [20]

$$u_1 = \frac{\theta_0'}{2} - \frac{\sin\theta_0}{2\rho}, \quad v_1 = \frac{\theta_0'}{2} + \frac{\sin\theta_0}{2\rho}, \qquad \omega_1 = 0. \quad (A.5)$$

A simple calculation shows that $C_1 = 0$, therefore the soliton motion is connected only with the mode $m = -1$, see equation (26).

Let us calculate the dynamics of the "guiding center" position of the soliton (27). Using the partial-wave expansion (24), one can rewrite the topological density $\mathcal{Q}$ (9) as follows:

$$\mathcal{Q} = -\frac{\sin\theta_0\,\theta_0'}{l_0^2\rho} - \frac{1}{l_0^2\rho}\sum_m A_m\cos\Phi_m\Big[(u_m'+v_m')\sin\theta_0$$
$$+(u_m+v_m)\cos\theta_0\theta_0' + m(u_m-v_m)\theta_0'\Big].$$

Averaging the linear momentum (27) with account of (A.2) one can derive $\boldsymbol{R}(t)$ in the form

$$\boldsymbol{R}(t) = l_0A_1C_1^\star + l_0A_1C_{-1}^\star\exp\left(-i\omega_{-1}t\right), \qquad (A.6)$$

where the constant $C^{\star}_m$ can be calculated as follows:

$$C^{\star}_m = \frac{1}{4}\int_0^{\infty} \rho d\rho \Big\{ (1+m)\Big(u_m u_1 - v_m v_1\Big) - (1-m)\Big(u_m v_1 - v_m u_1\Big)\Big\}.$$

Using explicit form (A.5) for the zero-frequency mode, one can easily see that $C^{\star}_1 = -1$, and the contribution of the mode $m = +1$ results in the soliton shift. For the mode with $m = -1$ one can rewrite the constant $C^{\star}_{-1}$ in the form:

$$C^{\star}_{-1} = \frac{1}{2}\int_0^{\infty} \rho d\rho \Big(u_{-1} v_1 - v_{-1} u_1\Big).$$

This integral vanishes due to the symmetry of the eigenvalue problem (25). Namely, a simple calculation shows that

$$\frac{\omega_m + \omega_{-m}}{\omega_0}\Big(u_m v_{-m} - v_m = u_{-m}\Big) = \boldsymbol{\nabla}\cdot\Big(u_m \boldsymbol{\nabla} v_{-m} + v_m \boldsymbol{\nabla} u_{-m} - u_{-m}\boldsymbol{\nabla} v_m - v_{-m}\boldsymbol{\nabla} u_m\Big)$$

for any m. The righthandside is in the form of the total divergence, thus it gives no contribution to the integral over the system:

$$\int_0^{\infty} \rho d\rho \,(u_m v_{-m} - v_m u_{-m}) = 0.$$

Therefore the constant $C^{\star}_{-1} = 0$, and finally the "guiding center" of the soliton can be rewriting in the form (28).

Appendix B: Parallelized computations

There exist two main possibilities of parallelization computations: (i) the usage of a vector-computing machine which has a shared memory or (ii) the usage of a cluster system (usually a Linux cluster) with communication between the different processors (nodes). The latter process is called *message passing interface* (MPI), this interface does not depend on the programming language.

In MPI there is a master-process which is responsible for the administration of the data, i.e. initializations, reading or saving of data, whereas the other nodes (slaves) are doing the calculation (e.g. integration). In our case we divide the lattice into horizontal stripes. As in our system we take into account nearest-neighbor interaction we must put a communication between the borders of the stripes. To make calculations for the ith stripe we need the lower border of the $(i+1)$th stripe and the upper boarder of the $(i-1)$th stripe. This exchange is done after every second integration step in the Runge Kutta algorithm. This advantages a good equilibrium between the latency period (time in which the nodes are synchronized), data-transferring time, and calculation time. As the boundary condition of our lattice is periodic the upper boarder of the top stripe is exchanged with the lower border of the bottom stripe. Concerning the left and right boarders of one stripe there are no communication processes, because horizontal cuts of the system advantage an internal exchange of the lateral borders in one process.

As the data is always transferred between the same nodes we implement a *persistant connection mode* in order to make the *overhead* (additional time spent on the connection establishment) smaller. Theses connections are built up at the beginning of the integration to be ready for a fast use.

The transfer takes place in an asynchronous, buffered mode. Thereby the data resulting of the calculation on a stripe is put into a buffer so that for this node there is no need to wait until the other nodes are ready to receive. In order to do a new calculation in the next time steps the stripe awaits information of its neighbored stripes. The advantage of this method is that the time exposure for the synchronization of the nodes decreases.

After integrating 40 time steps with $\Delta t = 0.01$ we calculate the soliton position $\boldsymbol{X}(t)$ discretely and optimally distributed over the other nodes. After finishing the calculations the data is sent from the slaves to the master-process which saves the data in a file.

The parallelizing of the source code is much easier and more effective if one can use shared memory multiprocessors machines. The loops are environed by sunstyle parallelization-directives. According to the dependency of the variables they have to be declared as *private variables* and others as *reduction variables*. *Private variables* take different values in different threads (such as auxiliary variables) so there is no shared memory for these variables. *Reduction variables* are used for sums which are distributed over different threads during one loop and are added in the end of the parallelized loop. The advantage of this method is a very fast access to the shared memory of all threads. This avoids a time consuming latency period caused by a communication process. To summarize we want to stress that a shared memory machine is always much faster than a cluster, if one considers a fixed number of processors to be in use. The only advantage a cluster has is the fact that compared to a shared memory machine it has much more processors and the number of processors can be increased arbitrarily. Also aspects of the price motivate universities and institutes to buy a cluster instead of a shared memory machine.

References

1. A.M. Kosevich, B.A. Ivanov, A.S. Kovalev, Phys. Rep. **194**, 117 (1990)
2. V.G. Bar'yakhtar, M.V. Chetkin, B.A. Ivanov, S.N. Gadetskii, *Dynamics of Topological Magnetic Solitons. Experiment and Theory* (Springer-Verlag, Berlin, 1994)
3. F.G. Mertens, A.R. Bishop, in *Nonlinear Science at the Dawn of the 21th Century*, edited by P.L. Christiansen, M.P. Soerensen, A.C. Scott (Springer-Verlag, Berlin, 2000)
4. V.L. Berezinskiĭ, Sov. Phys. JETP **34**, 610 (1972)
5. J.M. Kosterlitz, D.J. Thouless, J. Phys. C **6**, 1181 (1973)

6. A.A. Belavin, A.M. Polyakov, JETP Lett. **22**, 245 (1975)
7. R.H. Hobard, Proc. Phys. Soc. **82**, 201 (1963)
8. G.H. Derrick, J. Math. Phys. **5**, 1252 (1964)
9. V.G. Bar'yakhtar, B.A. Ivanov, Sov. Sci. Rev. Sec. A. **16**, 3 (1993)
10. V.G. Makhankov, Phys. Rep. **35**, 1 (1978)
11. H. Walliser, G. Holzwarth, Phys. Rev. B **61**, 2819 (2000)
12. *The quantum Hall effect*, edited by R.E. Prange, S.M. Girvin (Springer, New York, 1990)
13. B.A. Ivanov, H.J. Schnitzer, F.G. Mertens, G.M. Wysin, Phys. Rev. B **58**, 8464 (1998)
14. N. Papanicolaou, W.J. Zakrzewski, Physica D **80**, 225 (1995)
15. N. Papanicolaou, T.N. Tomaras, Nucl. Phys. B **360**, 425 (1991)
16. N. Papanicolaou, W.J. Zakrzewski, Phys. Lett. A **210**, 328 (1996)
17. B.A. Ivanov, V.A. Stephanovich, Phys. Lett. A **141**, 89 (1989)
18. C.E. Zaspel, Phys. Rev. B **48**, 926 (1993)
19. T. Kamppeter, S.A. Leonel, F.G. Mertens, M.E. Gouvêa, A.S.T. Pires, A.S. Kovalev, Eur. Phys. J. B **21**, 93 (2001)
20. D.D. Sheka, B.A. Ivanov, F.G. Mertens, Phys. Rev. B **64**, 024432 (2001)
21. A.S. Kovalev, A.M. Kosevich, K.V. Maslov, JETP Lett. **30**, 296 (1979)
22. A.M. Kosevich, V.P. Voronov, Sov. J. Low Temp. Phys. **7**, 442 (1981)
23. V.P. Voronov, B.A. Ivanov, A.K. Kosevich, Sov. Phys. JETP **84**, 2235 (1983)
24. B.A. Ivanov, V.A. Stephanovich, Sov. Phys. JETP **64**, 376 (1986)
25. D.D. Sheka, J.P. Zagorodny, J.G. Caputo, Y. Gaididei, F.G. Mertens, Phys. Rev. B **71**, 134420 (2005)
26. N.R. Cooper, Phys. Rev. Lett. **80**, 4554 (1998)